



LAWRENCE
LIVERMORE
NATIONAL
LABORATORY

LLNL-JRNL-410563

Overview of the results on divertor heat loads in RMP controlled H-mode plasmas on DIII-D*

M.W. Jakubowski, T.E. Evans, M.E. Fenstermacher, M. Groth, C.J. Lasnier, A.W. Leonard, O. Schmitz, J.G. Watkins, T. Eich, W. Fundamenski, R.A. Moyer, R.C. Wolf, L.B. Baylor, J.A. Boedo, K.H. Burrell, H. Frerichs, J.S. deGrassie, P. Gohi, I. Joseph, S. Mordijck, M. Lehnen, C.C. Petty, R.I. Pinsker, D. Reiter, T.L. Rhodes, U. Samm, M.J. Schaffer, P.B. Snyder, H. Stoschus, T. Osborne, B. Unterberg, E. Unterberg, W.P. West

February 13, 2009

Nuclear Fusion

Disclaimer

This document was prepared as an account of work sponsored by an agency of the United States government. Neither the United States government nor Lawrence Livermore National Security, LLC, nor any of their employees makes any warranty, expressed or implied, or assumes any legal liability or responsibility for the accuracy, completeness, or usefulness of any information, apparatus, product, or process disclosed, or represents that its use would not infringe privately owned rights. Reference herein to any specific commercial product, process, or service by trade name, trademark, manufacturer, or otherwise does not necessarily constitute or imply its endorsement, recommendation, or favoring by the United States government or Lawrence Livermore National Security, LLC. The views and opinions of authors expressed herein do not necessarily state or reflect those of the United States government or Lawrence Livermore National Security, LLC, and shall not be used for advertising or product endorsement purposes.

Overview of the results on divertor heat loads in RMP controlled H-mode plasmas on DIII-D*

M.W. Jakubowski^{1,2}, T.E. Evans³, M.E. Fenstermacher⁴, M. Groth⁴, C.J. Lasnier⁴, A.W. Leonard³, O. Schmitz², J.G. Watkins⁶, T. Eich¹, W. Fundamenski⁷, R.A. Moyer⁵, R.C. Wolf^d, L.B. Baylor³, J.A. Boedo⁵, K.H. Burrell³, H. Frerichs², J.S. deGrassie³, P. Gohil³, I. Joseph⁵, S. Mordijck³, M. Lehnen², C.C. Petty³, R.I. Pinsker³, D. Reiter², T.L. Rhodes⁵, U. Samm², M.J. Schaffer³, P.B. Snyder³, H. Stoschus², T. Osborne³, B. Unterberg², E. Unterberg³, W.P. West³

¹ Max-Planck-Institut für Plasmaphysik, IPP-EURATOM Association, Garching & Greifswald, Germany

² Institut für Energieforschung 4 – Plasmaphysik, Forschungszentrum Jülich, Association FZJ-

EURATOM, TEC, Jülich, Germany

³ General Atomics, P.O. Box 85608, San Diego, California, 92186-5608 U.S.A.

⁴ Lawrence Livermore National Laboratory, P.O. Box 808, Livermore, CA 94550, U.S.A.

⁵ University of California, San Diego, La Jolla, CA 92093, U.S.A.

⁶ Sandia National Laboratory, Albuquerque, New Mexico, U.S.A.

⁷ EURATOM/UKAEA Fusion Association, Culham Science Centre, Abingdon, Oxfordshire, UK

Abstract. In this paper the manipulation of power deposition on divertor targets at DIII-D by application of resonant magnetic perturbations (RMPs) for suppression of large Type-I edge localized modes (ELMs) is analysed. We discuss the modification of the ELM characteristics by the RMP applied. It is shown, that the width of the deposition pattern in ELMy H-mode depends linearly on the ELM deposited energy, whereas in the RMP phase of the discharge those patterns are controlled by the externally induced magnetic perturbation. It was also found that the manipulation of heat transport due to application of small, edge resonant magnetic perturbations (RMP) depends on the plasma pedestal electron collisionality. We compare in this analysis RMP and no RMP phases with and without complete ELM suppression. At high, the heat flux during the ELM suppressed phase is of the same order as the inter-ELM and the no-RMP phase. However, below this collisionality value, a slight increase of the total power flux to the divertor is observed during the RMP phase. This is most likely caused by a more negative potential at the divertor surface due to hot electrons reaching the divertor surface from the pedestal area along perturbed, open field lines and/or the density pump out effect.

1 Introduction

Large type-I Edge Localized Modes (ELMs) [1] are a significant concern in tokamak plasmas as they cause high, transient heat loads on the plasma facing components. They appear as a series of rotating filamentary structures [2] due to pedestal pressure gradients found at the edge of H-mode plasmas [3]. These ELM filaments form characteristic spiral heat load pattern on the divertor surface [4]. They have been successfully eliminated in H-mode plasmas at the DIII-D tokamak [5] by application of small, edge resonant magnetic perturbations (RMPs) produced by coils external to the plasma but inside the vacuum vessel over wide range of pedestal collisionalities and plasma shapes [6-8]. Currents flowing in the coils create a relatively small magnetic perturbation, which consists mainly of components with and is resonant to the $q=3$ flux surfaces, located at the plasma boundary for the plasmas investigated. Depending on the current

* Work supported by the US Department of Energy under DE-AC04-94AL85000, DE-AC52-07NA27344, DE-FC02-04ER54698 and DE-FG02-04ER54758.

distribution within the coils one can realize magnetic perturbation with different up/down symmetry. The parity of the coils is named ‘even’ when the upper and lower coils have the same polarity at each toroidal angle φ and ‘odd’ when these polarities are opposite.

The interaction of the RMP with magnetic equilibrium imposes a three-dimensional topology of perturbed magnetic field lines in the plasma edge [9]. Topologically, this volume consists of two layers:

1. An inner stochastic boundary, where the radial particle transport is potentially enhanced due to high diffusivity of magnetic field lines [10,11] and non-ambipolar particle transport for instance [12,13], is located near the pedestal area. It has been shown in [14] that the suppression of Type-I ELMs correlates with a minimum width of the edge region having magnetic islands with Chirikov parameter > 1.0 , based on vacuum calculations of RMP mode components excluding the plasma response or rotational shielding.
2. In a diverted tokamak, poloidal magnetic flux (ψ) escaping the outer edge of this stochastic region is organized by complex topological structures known in nonlinear dynamical systems theory as homoclinic tangles [15]. Such a tangle is generated by a splitting of the separatrix into a set of invariant manifolds when perturbed by small non-axisymmetric magnetic fields. At the separatrix a set of invariant manifolds is created, which forms a specific spiral pattern on the divertor surface. Lobes of the manifolds form an envelope for the open field lines leaving the stochastic area and intersecting the divertor target plates [16]. Those field lines are mixture of long connection length stochastic field lines and short connection length laminar field lines.

As the parallel transport exceeds by orders of magnitudes the perpendicular one, it is expected that during the RMP phase of the discharge the heat and particle flux on the divertor target plates should reflect this generic structure of the striated strike lines. This has been observed in different experiments including limiter [17-19] and divertor plasmas [15,20]. The aim of this paper is to discuss effects of the stochastic boundary at DIII-D on the heat loads to the divertor surface. It consists of two parts:

- In section 3, which follows discussion of the experimental set-up, we discuss the properties of ELM heat load deposition patterns and their modification by the external perturbation. The investigations have been performed in plasmas with ITER Similar Shape and electron pedestal collisionalities. It has been found, that the wetted area of ELMs during non RMP H-mode discharge depends on ELM size in terms of the power deposited to the inner divertor leg. This is consistent with recently proposed mechanism for ELM behaviour given in [21] that temperature losses due to an initial peeling-ballooning instability, conducted along opened magnetic field lines due to a small pre-existing perturbation leads to a temperature difference at the end point of the field lines at the inner and outer divertor targets. The resulting thermo-electric currents are supposed to be capable to amplify explosively the existing magnetic field perturbation. Moreover, we do see that remaining ELMs in the initial RMP phase, have very similar target power load deposition patterns. This suggests that ELMs are controlled by the external field and their power deposition patterns resemble the structure of magnetic footprints on the target calculated with the TRIP3D code [22].

This initial relatively short period, of RMP interaction with ELMs is followed by the phase when ELMs get completely eliminated. It is quite important for the ITER safety to understand how the power flux changes in this case. In section 4 we review the results of heat flux behaviour with the

RMP and compare them to non-RMP H-mode results for a wide range of pedestal electron collisionalities ν_{te} at high and low triangularity (including ITER-similar shapes). Here R is the major radius of the torus, a is the minor radius, κ is the inverse aspect ratio and λ_{te} – mean free path for electron collisions. This analysis includes the power balance, inner/outer leg asymmetries and structure of the strike lines. Switching on I-coils in plasmas with higher ν_{te} does not affect power deposited to the divertor independent on the I-coils parity. At ITER-like collisionalities we observe small increase of the heat flux to the target plates. Also, as expected, double null plasmas show higher asymmetries than single null discharges. Ratio of inner to outer power loads shows dependence on electron pedestal collisionality.

2 Experimental set-up

We examine in this paper both, quasi double-null plasma discharges at high ν_{te} with moderate to high triangularity δ as well as lower single null plasmas with low density, low ν_{te} (both low and high triangularity). The plasma shapes discussed within this work are presented in Figure 1. Between the 2005 and 2006 operating period the DIII-D lower cryopump baffle was extended, as shown in Figure 1c, to allow for optimized pumping in plasmas with higher triangularities – similar to those planned for ITER. All those discharges had slight variation in q_{95} in order to stay in the resonant window for magnetic perturbations, in which Type-I ELMs are completely suppressed [14]. The preferred diagnostic for divertor target heat load measurements is infra-red thermography. In this work the heat flux analysis has been performed with two infra-red cameras mounted at two different toroidal locations: 1) a fast-framing infra-red Santa Barbara Focal Plane (SBF-125) camera at toroidal angle of (-10°) with a time resolution of 13 kHz and spatial resolution of 5-7 millimetres per pixel on the target surface, and 2) the FLIR Systems Inc. infra-red camera located at toroidal angle (-10°) with 50 Hz time resolution and similar spatial resolution. Both cameras have a viewing geometry observing the lower divertor area; however in most cases they did not run simultaneously. The setup for the infrared camera SBF-125 is presented in Figure 2a. Both cameras observe the surface of the lower divertor using similar optics. As presented in Figure 2b a toroidal region of (-10°) centered at (-10°) is observed by the SBF system. At present in most plasma configurations only the inner strike line can be observed due to the shape of the pumping duct, which covers the outer strike line from the camera view. However for most of the discharges discussed in section 4 the infra-red data was taken with both strike lines visible due to a different geometry of the lower divertor shelf (see Figure 1a-b).

The heat fluxes on the target surfaces are calculated for the SBF-125 system by applying a standard numerical solution of the two-dimensional heat diffusion equations to the evolution of the surface temperature on the investigated area with the THEODOR code [23], while for the FLIR system a semi-infinite approximation for the heat diffusion in a solid bulk material is used. The THEODOR code [23], which is used to study heat loads due to Type-I ELMs has the ability to evaluate the influence of the surface layers on the evaluated heat flux density. The code starts from the temporal evolution of the surface temperature distribution along the poloidal target coordinate obtained with help of the LEOPOLD code [4] and computes the heat flux distribution using a 2D slab geometry approximation for the target tiles, introducing the real poloidal target width and an averaged target thickness. Front surface layers are taken into account with the heat transmission coefficient α , which is chosen in such a way that negative heat fluxes in the inter-ELM period are avoided. The coefficient assumes the same surface properties across the strike line, which is not necessarily correct, therefore some caution must be taken with absolute

numbers of the heat flux density. However, we took care to minimize the influence of the co-deposits on the analyzed data. A detailed discussion of the method on examples of ASDEX-Upgrade and JET data is given in [23,24]. In the section 7 we use low time resolution camera data to discuss global changes of the power flux caused by the RMP, therefore a semi-infinite approximation, which does not take into account surface layers is sufficient. Additionally, the data is checked against global power balance; we find fair agreement between heat flux obtained from both methods.

3 Influence of RMP on ELM deposition patterns

It has been reported from ASDEX-Upgrade, that Type-I ELMs create helical footprint patterns of heat flux on the divertor surface [4]. Several strike lines were detected outside the original strike point of the outer leg albeit at very low amplitude. They form helically aligned structures, which are clearly related to the topology of the magnetic field. In this work we have found very similar structures on the inner and outer target plates. However, as most of the area of the outer strike point is hidden from the infrared camera by the vessel structures, we will concentrate on the substructures detected during ELM events on the inner target plates of an H-mode discharge. The investigated discharges have been performed at low pedestal collisionality () and ITER-like plasma shapes ().

An example of the scenario is given in **Error! Reference source not found.** Figure 3. At ms there is a transition to ELMy H-mode associated by a mixture of large Type-I ELMs with frequency of about 50 Hz and small ones (probably Type-II ELMs). The maximum power load to the inner target during an ELM can reach up to 15 MW for the largest Type-I ELMs and about 2-3 MW for the smaller ELMs. Switching on the I-coil current of 4.5 kA at first makes ELMs more frequent (~200 Hz) and changes their amplitudes. Peak heat flux due to Type-I ELMs decreases roughly by factor of 3 and due to Type-II increases by factor of 2. Shortly before $t = 2400$ ms all instabilities disappear completely. Small ELM-like bursts at $t \approx 2500$ ms are caused by pellets injected into the plasma. They do not appear in every discharge and have amplitudes slightly smaller than ELMs in the initial RMP phase, i.e. much smaller than the ELMs without the RMP.

3.1 Basic properties of ELMs

Before discussing ELM deposition patterns during the initial RMP phase, we present observations from the non-RMP H-mode phase of the discharge inspected. An example of an infrared image taken by the SBFP camera of the substructures during an ELM without the RMP is shown in Figure 4**Error! Reference source not found.** Three additional strike lines are visible in the remote area of the inner strike line (upper, right part of the image). Usually, there are two to five non-axisymmetric strike lines observed at the inner strike point position during an ELM event. Their width is typically in the range of 2 – 4 cm and the separation between them is of the same order. The grid projected onto the image shows the vessel model applied in the LEOPOLD code [4] to unfold the temperature data.

For the purpose of this work we have performed calculations in the area indicated by two yellow dashed lines. Temperature data have been obtained with very good time resolution ($f=13\text{kHz}$), which allowed to study the evolution of the structures during an ELM event. Two examples are shown in Figure 5**Error! Reference source not found.** In the example on the left hand side – at the ELM onset ($t = 1961$ ms, #129197) two strike lines appear (at $s - s_0 \approx 20$ mm and $s - s_0 \approx 60$ mm) with the latter one depositing most of the heat to the target. At a time $190 \mu\text{s}$ later, a third substructure (at $s - s_0 \approx 120$ mm) appears, which lasts only until the heat flux deposition gets to its

maximum at $\Delta t = 360 \mu\text{s}$. After another $150 \mu\text{s}$ the main strike line and the second lobe show no changes of their structures anymore and decay within 2 ms to the pre-ELM values. For some of the ELM events there is a clear signature of the lobes separation, which suggests toroidal rotation of the structures. An example of such behavior is shown in Figure 5**Error! Reference source not found.**b. The time scales of the events recorded by the camera are very similar to the previous case, the difference is however in the internal evolution of the substructures. Here we observe an increasing separation of the main strike line and the second lobe from to within the time frame of $100 \mu\text{s} < \Delta t < 500 \mu\text{s}$, at the end of which the peak heat load reaches its maximum of 7 MW/m^2 . As we expect that the ELM filaments produce spiraling patterns on the target [25], an increase of the separation of the lobes is consistent with a toroidal movement of the striated patterns. After $\Delta t = 500 \mu\text{s}$ again we do not see any evolution of the pattern on the target, but only a decay of the heat load to the pre-ELM state.

The energy deposited to the inner target per ELM for all investigated ELMs is presented in Figure 6 as a function of the time of the ELM event**Error! Reference source not found.**. Each point represents the energy deposited to the inner target during one event. It is calculated with the following formula

$$E_{\text{ELM}} = \int_{s_0}^{s_n} \int_{t_0}^{t_n} q(s, t) ds dt, \quad (3.1)$$

where $q(s, t)$ is the heat flux density, s_0 and s_n define spatial limits for the integration, t_0 and t_n – starting and ending time point of single ELM event. E_{base} is the inter-ELM power to the target, which would be deposited to the inner target if there would be no ELM in this time range; it is interpolated from $E(t_0)$ and $E(t_n)$. Results reveal two groups of data points, which are well separated from each other and marked with blue and red circles. These are identified as Type-I and, probably, Type-II ELMs respectively. The latter ones, as expected, deposit much smaller energy to the inner target (below 10 kJ). Before the RMP phase ($t < 2200 \text{ ms}$) one observes an increasing amount of energy deposited to the target per ELM for $1200 \text{ ms} < t < 2100 \text{ ms}$. This is caused by increasing heating power from the neutral beam injection, which reaches a maximum of 9 MW at $t \approx 2100 \text{ ms}$. At this time the energy deposited per ELM reaches 40 kJ for Type-I and a few kJ for Type-II ELMs. Application of RMP at $t = 2200 \text{ ms}$ reduces the amount of energy deposited per event for Type-I ELMs to the value in the range of 20 – 30 kJ. Surprisingly, Type-II ELMs deposit more energy with the magnetic perturbation (5-10 kJ) than without the RMP. Bursts caused by the injection of D_2 pellets recreate both types of ELMs for a short period of time at $t \approx 2500 \text{ ms}$. In this shot they deposit the power to the divertor in the same ranges as ELMs in the initial RMP phase and will be discussed in the last paragraph of this work.

3.2 Variation of ELM deposition footprints with ELM size

One of the recent ideas [21], which still needs experimental confirmation, about the evolution of the Type-I ELMs assumes that the transient event is initiated when a peeling-ballooning mode gets destabilized as the pedestal pressure gradient exceeds the linear marginal stability limit of the mode [26]. This produces an initial pulse of heat and particles that propagates radially outward into a small pre-existing homoclinic separatrix tangle. Due to different parallel connection length from the outboard midplane to the targets increase of the electron temperature is higher at the outer strike point than at the inner one, which leads to the onset of thermoelectric currents within the filaments [13,18]. As the filaments have helical forms, their currents should create a magnetic perturbation, which also has components that are resonant to the edge magnetic

equilibrium [13,15]. It has been shown that divertor heat flux and particle recycling patterns are consistent with magnetic footprints produced by separatrix splitting associated with homoclinic tangles under some conditions [9,22]. Since homoclinic tangles result naturally from a variety of stationary and/or time dependent non-axisymmetric magnetic perturbations that are found in any realistic tokamak due to many sources of field errors [22,27,28], it is not unreasonable to expect these structures to be the norm rather than the exception, also during the on-set of an ELM. These components should create at least a temporal perturbation of the separatrix, which is consistent with the observed splitting of the separatrix during ELMs. Intuitively, one would expect that larger ELMs should carry larger currents, which would eventually lead to the greater splitting of the separatrix as compared to small ELMs. This is actually consistent with the experimental findings as presented below. The width of an ELM deposition pattern is defined here as

$$\text{width} = \frac{\int_{-\infty}^{\infty} q(s) ds}{\max(q(s))} \quad [m], \quad (3.2)$$

where q [MW/m²] is the heat flux density profile taken at the time when the heat load to the divertor reaches its maximum (), s [m] – is the coordinate along the divertor contour, and $\max(q(s))$ denotes the maximum of the heat flux density profile. ELM wetted area, i.e. area, where the heat flux is deposited is proportional to (with R being major radius of the strike line). The dependence of w_f on ELM size, expressed as a function of deposited energy E_{dep} , is shown in Figure 7 **Error! Reference source not found.**. There is a clear increase of the width versus the amount of energy deposited per ELM from about 4 cm for Type-II ELMs (<10 kJ) to about 8 cm for the largest Type-I ELMs. This increase seems to have a linear characteristic and the values are slightly smaller than the profile widths at the half-maximum. Profiles of deposited power for different ELMs are presented in Figure 8 **Error! Reference source not found.**. They are ordered according to the energy deposited to the target (the abscissa) and normalized to the maximal value for each of the profiles. Here again, one recognizes increasing width of the deposition pattern with the ELM size. It is interesting to note that for virtually all ELMs below 15 kJ there are two substructures visible. Their splitting increases from 3 cm at $E_{\text{dep}} = 2\text{-}3$ kJ to 8 cm at $E_{\text{dep}} = 15$ kJ. Larger instabilities show more random structuring, with 2 to 4 or even 5 substructures. This variability is caused most like by a different toroidal phase of the footprint at the moment of detection and/or different shape of the perturbation spectrum.

A very interesting change in ELM behavior happens, when the $n=3$ RMP plasma operation is considered (red dots in Figure 7 **Error! Reference source not found.**). For both types of ELMs w_f becomes less scattered ($w_f \approx 3\text{-}4$ cm and 7 cm respectively) and narrower, when compared to the same energies in the non-RMP case. Their structure became almost the same – all instabilities with energy deposited below 15 kJ do not have any additional substructure. Almost all above 20 kJ have three deposition lobes with the distance along them not varying with the energy. This probably means that structure of the separatrix is dominated by the magnetic perturbation coming from the I-coils, i.e. that the radial magnetic component of the magnetic field induced by 4 kA I-coil current is much stronger, than b_r induced by currents flowing within the filaments. Indeed, measurements performed on TEXT have shown that filaments can carry currents of order of hundreds of Amperes [provide reference!]. The heat pulse due to ELMs travelling across the separatrix is diverted along the open field lines of the stochastic boundary to the target plates and deposited through the lobes of the separatrix. Figure 9 **Error! Reference source not found.** shows a comparison of the measured heat flux density profile with predictions of the structure of target patterns from TRIP3D. When we compare the deposition profile of Type-I ELM with the

topology of magnetic footprints we find fair agreement between both structures. Additionally those structures do not show the same dynamics as ELMs in the non-RMP phase of the discharge. Figure 10**Error! Reference source not found.** depicts an example of the power deposition pattern during a Type-I ELM in the same manner as in Figure 5**Error! Reference source not found.**. The heat pulse reaches first the main strike line and after 100 μs simultaneously two lobes at mm and mm . All three hot spots reach their maximum at ms , i.e. about 200 μs earlier as in the examples during the non-RMP phase (see Figure 10**Error! Reference source not found.**). In contrary to non-RMP results from Figure 5, here we do not observe changes of the hot spots structure. Energy deposition through the external substructures decays much faster as for the main strike line. They show no signature of any filament rotation, which suggests locking of ELMs to the external perturbation. For all investigated instabilities the maximum of the power deposition falls into the main strike line and decays with increasing distance from the separatrix. This picture qualitatively resembles results of numerical modeling of heat transport in weakly stochastic fields performed with EMC3-EIRENE [9] and E3D [30] codes. Both codes predict “filling” of the outer separatrix lobes with energy coming from the pedestal by stochastic field lines in the case of static magnetic perturbations. This is consistent with the hypothesis presented above about the stochastic nature of the heat transport during an ELM. Most likely there is a positive coupling of the resonant magnetic components coming from the filament currents and the I-coils, what enhances the heat transport through the pedestal. One should note that the ratio of power deposited through the outer lobe to the main strike line is much higher than in the case of the ELM-free RMP phase of the discharge (see Figure 15).

4 Heat flux to the divertor at different collisionalities

High and low ν_{ei} discharges show different behaviour of the heat flux to the divertor during ELM suppression. Two examples are presented in Figure 11, where time traces for #119692 and #126006 are presented. The discharges are performed with upper and lower triangularity of () and () respectively. In both cases the I-coils have been run with almost the same current of 4 kA. The currents have been run with either even (#126006) or odd (#119692) parity. Width of the stochastic boundary, as calculated in vacuum approach, should not depend on the parity of the I-coil currents.

In the high ν_{ei} case (black curves in Figure 11) ELMs are suppressed immediately after the I-coils are switched on ($t = 3000 \text{ ms}$). There is no significant effect on the energy deposited to the target plates of the lower divertor during the whole RPM phase. As the diamagnetic energy is not affected by stochastization of the plasma boundary, there is also no temporary increase of the deposited energy due to a heat pulse crossing the separatrix. As reported in [31], at high collisionalities, the floating potential (V_f) measured by the divertor Langmuir probes near the outer strike point is approximately zero during application of the RMP, suggesting a drop of the temperature in the scrape-off layer and weaker acceleration of ions towards the target by the sheath due to RMP application. For discharge #119692, the floating potential increases from slightly above zero to a few volts as shown in Figure 12, black curve, i.e. there is no significant change of sheath properties.

Contrary results are obtained for low collisionality discharges (e.g. #126006 in Figure 11) – ELM suppression by the RMP is associated with a density pump-out and a small drop of the diamagnetic energy. As the confinement drops there is an additional portion of energy leaving the plasma, which is immediately seen as a 50% increase of the total heat flux to the divertor. After the energy confinement reaches its new equilibrium, the energy deposited to the divertor remains on a higher level as compared to the non-RMP phase (7 MW in #126006 as compared to 6 MW in pre-RMP phase). This increase of the heat flux is observed for all investigated discharges with $\nu_e^* < 3$ at DIII-D. It is accompanied by the fact that the floating potential at the position of the strike point becomes strongly negative as illustrated in Figure 12, which suggests interaction of hot electrons with the surface of the target plates. Most likely these electrons come from the pedestal area along the magnetic field lines perturbed by the RMP and at low ν_e^* they are almost collisionless. Conversely, at $\nu_e^* = 3$ or 4 they are not able to reach to the sheath area from the pedestal, i.e. the hot electrons are more likely to dissipate energy before reaching the surface of the targets. A more negative floating potential enhances the transfer of energy to ions and thus increases the heat flux to the surface. For all the investigated cases with $\nu_e^* > 3$ independent on the parity of the I-coils, there is no permanent increase of the heat flux. Figure 13 illustrates the changes in the power reaching the divertor (P_{target}) and the radiated power (P_{rad}) normalized to the total heating power (P_{total}) when the I-coils are energized. The power to the target is obtained using the equation:

$$\frac{P_{\text{target}}}{P_{\text{total}}} = \frac{W_{\text{dia}}}{W_{\text{dia}} + P_{\text{total}} t}, \quad (7.1)$$

where W_{dia} is the diamagnetic stored energy. For all the cases, where inner and outer legs could be observed by the infrared camera (e.g. #119692 - Figure 13a), there is a very good agreement between P_{target} and power to the divertor measured by the camera. At low collisionality, before the RMP phase, about 70% of the total energy is deposited to the target. This amount is increased by about 15% (to 80% of total heating power) after the I-coils are energized; at the same time radiated power drops from 25% to 20% of P_{tot} . The situation changes for higher ν_e^* – there both P_{target} and P_{rad} exhaust a similar fraction of energy, which is not affected by the RMP. The exact values of the radiated power are given in Table 1.

Volume	#119692 ()		#126006 ()	
	t = 2600 ms (no RMP)	t = 3750 ms (RMP)	t = 1775 ms (no RMP)	t = 2500 (RMP)
Core	0.63 MW	0.84 MW	0.54 MW	0.69 MW
SOL	0.33 MW	0.39 MW	0.42 MW	0.23 MW
Lower divertor (inner leg)	0.42 MW	0.37 MW	0.50 MW	0.41 MW
Lower divertor (outer leg)	0.53 MW	0.53 MW	0.30 MW	0.22 MW
Upper divertor (inner leg)	0.04 MW	0.04 MW	–	–
Upper divertor (outer leg)	0.14 MW	0.09 MW	–	–
Total	2.09 MW	2.26 MW	1.75 MW	1.55 MW

Table 1. Overview of the changes in the radiated power due to RMP for the discharges #119692 and #126006. The values are obtained from bolometric data and have about 10% error bar.

In both cases I-coil currents cause an enhancement of radiation by roughly 30% in the plasma core. The difference is clearly visible at the plasma boundary, where in high collisionality case radiated power is slightly increased in the scrape-off layer and almost not affected in the divertor volume. At low collisionality we observe about 50% (0.2 MW) drop of P_{rad} in the scrape-off layer and about 25% (0.2 MW) in the divertor area. All these findings indicate that the sheath properties are changed by application of RMP leading to the enhancement of the energy transfer to the target plates. A lower floating potential leads to a higher rate of energy deposited by the ions in the sheet and decreases the radiated power in the scrape-off layer. At higher collisionalities high energy electrons dissipate energy by collisions and do not affect the sheet potential so effectively. Thus the total amount of power deposited to the divertor surface is not affected by the RMPs. Probably, the pre-RMP ratio of Γ_{ion} and Γ_{e} in low collisionality discharges can be maintained during the RMP phase by seeding of a small fraction of impurities, which would enhance radiation in the divertor area.

4.1 Properties of the inner and outer strike lines in ELM suppressed phase of the discharge.

As mentioned already in Section 1, application of any non-axisymmetric perturbation removes degeneration of the separatrix manifolds, what is often referred to in the literature as a splitting of the strike line. It has been reported previously that the particle flux, contrary to the heat flux, almost always creates measurable signature of the perturbed strike line striation (see e.g. [9]). For the discharges investigated in this work, we observe that the structure of the heat flux profiles on the divertor surface changes with the pedestal collisionality, which has been observed as well in limiter plasmas at TEXTOR [32]. Figure 14a shows profiles of normalized heat flux density measured at the location of the outer strike point during the RMP phase at four different pedestal collisionalities. It is apparent that at high $n=3$ an additional lobe of the strike zone appears, when the $n = 3$ perturbation is applied. It has been found that there is only a clear splitting of the separatrix visible in the heat flux at high collisionalities (e.g. #119692). However, as discussed in [33] the separation of the lobes is 2-3 times larger than anticipated by the TRIP3D calculations [34] depicted for the high $n=3$ case (#119692) in Figure 14b and for the low $n=3$ case in Figure 14c. In the latter case, only very small heat fluxes [10] and in the actual example no heat flux at all is seen to be channeled along the perturbed separatrix lobes although they are separated by a rather huge distance of 1.5 cm each (see Figure 14c).

These results suggest that the plasma response to the applied $n=3$ edge resonant magnetic perturbation may amplify the effects of the external perturbation in terms of perturbation of the separatrix manifolds. This has two effects on the power deposition pattern to the divertor:

- a. Amplification of the separatrix deformation, i.e. wider splitting of the strike line than predicted from the vacuum magnetic field modeling.
- b. Possible enhanced coupling of the outer lobes to the pedestal by deeper penetration of magnetic field lines, which results in higher heat deposited through the outer lobes. One should note, that enhanced heat flux in the outer lobe also happens during discharges affected by locked modes in the plasma core and (as discussed in the next section) during ELMs.

At lower collisionalities (e.g. #123301) the width of the heat flux profile (~ 5 cm) corresponds roughly to the structure of the outer strike point (see Figure 14c) calculated by the TRIP3D code, which has about 3 cm width at $\varphi = 60^\circ$. As the thermographic system has a spatial resolution of order 1 cm, it is not possible to evaluate the internal structure of the strike point. However, recent

measurements with higher spatial resolution show that the outer lobe of the inner strike line during discharges with $n_{e0} = 1.5$ can be resolved experimentally, but with a low amount of the heat deposited there. This is presented in Figure 15, which is reproduced from [9]. This scenario utilizes plasma with ITER Similar Shape and ITER-like electron pedestal collisionality, and with I-coil currents of 4 kA. An overlapping region on the lower divertor surface is observed simultaneously using a CCD camera with a set of filters suitable to get spectral lines strongly related to the incoming particle flux and the IR camera SBF-125. Direct comparison of particle fluxes with the connection length profile shows three lobes of the striated strike line, with a shape in good agreement to the TRIP3D predicted structure of magnetic footprints, what is consistent with TEXTOR results on the stochastic boundary [32,35]. In the heat flux (Figure 15c) only the innermost of the separatrix lobes forms a large local heat flux maximum. The second lobe, detected well in particle flux, is hidden in the shoulder of the main heat flux peak, and the third lobe carries a power load with a peak value of about 0.4 MW/m^2 . As discussed in [9] these results confirm thermal connection between plasma pedestal and the target plates with relatively short connection length field lines.

4.2 Target energy deposition in/out asymmetry

It is a well known effect in poloidally diverted tokamaks that there is a power load asymmetry between the inner and outer leg of the divertor. For the inter-ELM heat loads this is caused by the drifts, ballooning transport on the low field side and geometrical effects [36,37]. Results from JET [24] show that the power loads of low triangularity discharges are almost identical to both legs of the divertor at pedestal collisionalities below 0.1 ($n_{e0} = 1.5$), while the ratio of the powers to the inner and outer leg of the divertor decreases to a value of 0.5 at a electron pedestal collisionality of 0.5. In this section we study the asymmetry in the ELM suppressed phase of the discharge. The results are shown in Figure 16. The data have been obtained for plasmas with either high (open points) or low triangularity (closed points). The general tendency is that the low triangularity plasmas show lower asymmetries as the discharges with high triangularity. This is not a surprising result as high triangularity plasmas are quasi double null plasmas. This results in some power deposition on the plasma facing components of the upper divertor due to the ballooning which localizes the transport rather on the low field side. Here we do observe that about 30 – 40% of the total deposited power goes to the inner target plate at pedestal collisionalities of order of 0.2 – 0.4. There is no any clear tendency here to be observed as the data have rather large scatter. The values are of the same order as the results from JET [24] for the inter-ELM phase; however we do not observe such a strong dependence on electron pedestal collisionality.

As already stated above, high triangularity plasmas show larger asymmetries between inner and outer power loads due to part of the energy deposited on the plasma facing components of the upper divertor. At $n_{e0} = 1.5$ about 20% of the deposited power goes to the inner target plate. In order to check the power balance we have calculated here also the in/out asymmetry for the discharge #126006, where we do not observe the outer strike zone. As the shape of the plasma has only lower single null, we assume that no power is deposited here to the upper divertor. The value of the energy deposited to the lower outer divertor has been obtained from the following equation:

$$(7.2)$$

where P_{out} is power deposited to the outer target, P_{div} total power to the divertor obtained from the power balance equation (7.1) and P_{in} is obtained from the heat flux to the inner target plates measured by the infra-red camera. The data point is marked as circle in Figure 16 and coincides quite well with the other data points for this plasma shape. As we slightly overestimate heat loads to the outer strike point adding there also all the power deposited to the upper divertor, we do expect that this data point would have a little bit higher value of the asymmetry factor. At $n_{e0} = 1.5 \times 10^{20} \text{ m}^{-3}$ we observe that about 90% of power coming to the target is deposited through the outer strike zone.

5 Summary

Achieving a tolerable heat loads to the plasma facing components are one of the key questions for the safety operation of future fusion devices like ITER or DEMO. At present As one of the most promising methods to control the power exhaust in poloidally diverted tokamak is the application of RMP, we have performed a review of the experimental results on the heat loads to the lower divertor obtained in DIII-D for different plasma configurations including low and high triangularities and for different electron pedestal collisionalities.

Independent on the plasma triangularity all discharges at electron pedestal collisionality below 0.5 show a slight (about 15% of the total power) increase of the heat flux to the target plates. This seems to be caused by a strong decrease of the floating potential due to very hot electrons from the pedestal area hitting the divertor surface. At very low n_{e0} the hot electrons are able to follow the stochastic field lines up to the target plates. A lower floating potential leads to a higher power deposited by the ions in the sheet and decreases the radiated power in the scrape-off layer. At higher collisionalities, high energy electrons dissipate their energy by collisions and do not affect the sheet potential. As a consequence, the total amount of power deposited to the divertor surface is not affected by the RMPs, but we have measured very strong asymmetries between power loads to the inner and outer target.

Also at high collisionalities we observe very clearly striation of the outer strike point with the separation of the lobes strongly exceeding results of the TRIP3D code. The power deposited through the second lobe sometimes exceeds the amount of energy deposited through the main strike line. Both these findings suggest enhancement of the external perturbation by its interaction with the plasma. Unfortunately, we still do not fully understand the nature of this coupling, but it is possible that the RMP induces additional currents on the resonant surfaces in the edge. Depending on the relative frequency of the RMP and electron diamagnetic drift frequency they can either suppress or amplify the stochasticization of the plasma boundary. At low collisionalities heat and particle flux patterns match, at least qualitatively, with calculated in vacuum magnetic topology of magnetic footprints. Here the asymmetry of power loads between inner and outer target is smaller as compared to higher pedestal collisionalities.

One of the most critical issues for ITER is formed by the transient heat loads to the divertor surface. At DIII-D experiments in ITER Similar Shape and with ITER-like electron pedestal collisionalities show linear dependence of the ELM wetted area on the ELM size. By wetted area we understand the size of the surface, where most of the heat load is deposited. All Type-I ELMs show dynamically evolving structures in the first few hundreds of microseconds until the heat loads reach their maximum. Typically, we do observe a few additional substructures separated from each other by 2-3 cm. After reaching a maximum in the deposited power, the target power does not show any changes of the internal substructures, but decay within 1 ms to the pre-ELM

values. In the initial RMP phase, where still few, smaller ELMs remain, we observe different behavior of the deposition patterns. Small, probably Type-II ELMs deposit all their energy through the main strike line. On the other hand, Type-I ELMs show two additional lobes with separation from the main strike line in very good agreement with the structure of the strike point at this toroidal angle as predicted by vacuum modeling. They also show no evolution characteristic for the ELMs in the non-RMP phase, which suggests locking of ELMs to the external perturbation. Wetted area is also independent on the ELM size.

6 Bibliography

- [1] H. Zohm, Plasma Physics and Controlled Fusion 38 (1996) 105-128.
- [2] A. Kirk, B. Koch, R. Scannell, H.R. Wilson, G. Counsell, J. Dowling, A. Herrmann, R. Martin, M.W.M. team, Phys. Rev. Lett. 96 (2006) 185001-4.
- [3] F. Wagner, M. Hirsch, H. Hartfuss, H.P. Laqua, H. Maassberg, Plasma Physics and Controlled Fusion 48 (2006) A217-A239.
- [4] T. Eich, A. Herrmann, J. Neuhauser, R. Dux, J.C. Fuchs, S. Günter, L.D. Horton, A. Kallenbach, P.T. Lang, C.F. Maggi, M. Maraschek, V. Rohde, W. Schneider, T.A.U. Team, Plasma Physics and Controlled Fusion 47 (2005) 815-842.
- [5] J. Luxon, Nuclear Fusion 42 (2002) 614-633.
- [6] K.H. Burrell, T.E. Evans, E.J. Doyle, M.E. Fenstermacher, R.J. Groebner, A.W. Leonard, R.A. Moyer, T.H. Osborne, M.J. Schaffer, P.B. Snyder, P.R. Thomas, W.P. West, J.A. Boedo, A.M. Garofalo, P. Gohil, G.L. Jackson, R.J.L. Haye, C.J. Lasnier, H. Reimerdes, T.L. Rhodes, J.T. Scoville, W.M. Solomon, D.M. Thomas, G. Wang, J.G. Watkins, L. Zeng, Plasma Physics and Controlled Fusion 47 (2005) B37-B52.
- [7] R.A. Moyer, T.E. Evans, T.H. Osborne, P.R. Thomas, M. Becoulet, J. Harris, K. Finken, J.A. Boedo, E.J. Doyle, M.E. Fenstermacher, P. Gohil, R.J. Groebner, M. Groth, G.L. Jackson, R.J. La Haye, C.J. Lasnier, A.W. Leonard, G.R. McKee, H. Reimerdes, T.L. Rhodes, D.L. Rudakov, M.J. Schaffer, P.B. Snyder, M.R. Wade, G. Wang, J.G. Watkins, W.P. West, L. Zeng, Phys. Plasmas 12 (2005) 056119-11.
- [8] T. Evans, M. Fenstermacher, R. Moyer, T. Osborne, J. Watkins, P. Gohil, I. Joseph, M. Schaffer, L. Baylor, M. Bécoulet, J. Boedo, K. Burrell, J. deGrassie, K. Finken, T. Jernigan, M. Jakubowski, C. Lasnier, M. Lehnen, A. Leonard, J. Lonnroth, E. Nardon, V. Parail, O. Schmitz, B. Unterberg, W. West, Nuclear Fusion 48 (2008) 024002.
- [9] O. Schmitz, T.E. Evans, M.E. Fenstermacher, H. Frerichs, M.W. Jakubowski, M.J. Schaffer, A. Wingen, W.P. West, N.H. Brooks, K.H. Burrell, J.S. deGrassie, Y. Feng, K.H. Finken, P. Gohil, M. Groth, I. Joseph, C.J. Lasnier, M. Lehnen, A.W. Leonard, S. Mordijck, R.A. Moyer, A. Nicolai, T.H. Osborne, D. Reiter, U. Samm, K.H. Spatschek, H. Stoschus, B. Unterberg, E.A. Unterberg, J.G. Watkins, R. Wolf, T. DIII-D, T. Teams, Plasma Physics and Controlled Fusion 50 (2008) 124029.
- [10] M.W. Jakubowski, O. Schmitz, S.S. Abdullaev, S. Brezinsek, K.H. Finken, A. Kramer-Flecken, M. Lehnen, U. Samm, K.H. Spatschek, B. Unterberg, R.C.W.T. Team, Phys. Rev. Lett. 96 (2006) 035004-4.
- [11] M. Schaffer, J. Menard, M. Aldan, J. Bialek, T. Evans, R. Moyer, Nuclear Fusion 48 (2008) 024004.
- [12] M.Z. Tokar, A. Gupta, Phys. Rev. Lett. 99 (2007) 225001-4.
- [13] A. Wingen, K.H. Spatschek, Phys. Plasmas 15 (2008) 052305-8.

- [14] M. Fenstermacher, T. Evans, T. Osborne, M. Schaffer, M. Aldan, J. Degraessie, P. Gohil, I. Joseph, R. Moyer, P. Snyder, R. Groebner, M. Jakubowski, A. Leonard, O. Schmitz, *Physics of Plasmas* 15 (2008).
- [15] T.E. Evans, R.K.W. Roeder, J.A. Carter, B.I. Rapoport, M.E. Fenstermacher, C.J. Lasnier, *Journal of Physics: Conference Series* 7 (2005) 174-190.
- [16] S. Abdullaev, K. Finken, M. Jakubowski, M. Lehnen, *Nuclear Fusion* 46 (2006) S113-S126.
- [17] F. Nguyen, P. Chendrih, A. Grosman, *Nuclear Fusion* 37 (1997) 743-757.
- [18] P. Ghendrih, A. Grosman, H. Capes, *Plasma Physics and Controlled Fusion* 38 (1996) 1653-1724.
- [19] M. Jakubowski, S. Abdullaev, K. Finken, T.T. Team, *Nuclear Fusion* 44 (2004) S1-S11.
- [20] O. Schmitz, T.E. Evans, M.E. Fenstermacher, H. Frerichs, M.W. Jakubowski, M.J. Schaffer, A. Wingen, W.P. West, N.H. Brooks, K.H. Burrell, J.S. deGrassie, Y. Feng, K.H. Finken, P. Gohil, M. Groth, I. Joseph, C.J. Lasnier, M. Lehnen, A.W. Leonard, S. Mordijck, R.A. Moyer, A. Nicolai, T.H. Osborne, D. Reiter, U. Samm, K.H. Spatschek, H. Stoschus, B. Unterberg, E.A. Unterberg, J.G. Watkins, R. Wolf, T. DIII-D, T. Teams, *Plasma Physics and Controlled Fusion* 50 (2008) 124029.
- [21] T. Evans, J.H. Yu, M.W. Jakubowski, O. Schmitz, J.G. Watkins, R.A. Moyer, *Journal of Nuclear Materials* to be published (n.d.).
- [22] T.E. Evans, R.K.W. Roeder, J.A. Carter, B.I. Rapoport, *Contributions to Plasma Physics* 44 (2004) 235-240.
- [23] A. Herrmann, W. Junker, K. Gunther, S. Bosch, M. Kaufmann, J. Neuhauser, G. Pautasso, T. Richter, R. Schneider, *Plasma Physics and Controlled Fusion* 37 (1995) 17-29.
- [24] T. Eich, P. Andrew, A. Herrmann, W. Fundamenski, A. Loarte, R.A. Pitts, J. contributors, *Plasma Physics and Controlled Fusion* 49 (2007) 573-604.
- [25] T. Eich, A. Herrmann, J. Neuhauser, *Phys. Rev. Lett.* 91 (2003) 195003.
- [26] H.R. Wilson, S.C. Cowley, *Phys. Rev. Lett.* 92 (2004) 175006.
- [27] M. Jakubowski, A. Wingen, S. Abdullaev, K. Finken, M. Lehnen, K. Spatschek, R. Wolf, *Journal of Nuclear Materials* 363-365 (2007) 371-376.
- [28] A. Wingen, M. Jakubowski, K.H. Spatschek, S.S. Abdullaev, K.H. Finken, M. Lehnen, T. team, *Phys. Plasmas* 14 (2007) 042502-7.
- [29] T.E. Evans, C. Lasnier, D.N. Hill, A.W. Leonard, M.E. Fenstermacher, T.W. Petrie, M.J. Schaffer, *J. Nucl. Mater.* 220-222 (1995) 235-239.
- [30] I. Joseph, T. Evans, A. Runov, M. Fenstermacher, M. Groth, S. Kasilov, C. Lasnier, R. Moyer, G. Porter, M. Schaffer, R. Schneider, J. Watkins, *Nuclear Fusion* 48 (2008) 045009.
- [31] J.G. Watkins, T.E. Evans, C. Lasnier, R.A. Moyer, D.L. Rudakov, *Journal of Nuclear Materials* 363 - 365 (2007) 708 - 712.
- [32] M.W. Jakubowski, M. Lehnen, K.H. Finken, O. Schmitz, S.S. Abdullaev, B. Unterberg, R. Wolf, *Plasma Physics and Controlled Fusion* 49 (2007) S109-S121.
- [33] T. Evans, I. Joseph, R. Moyer, M. Fenstermacher, C. Lasnier, L. Yan, *Journal of Nuclear Materials* 363-365 (2007) 570-574.
- [34] T.E. Evans, R.A. Moyer, P. Monat, *Phys. Plasmas* 9 (2002) 4957-4967.
- [35] O. Schmitz, M.W. Jakubowski, H. Frerichs, D. Harting, M. Lehnen, B. Unterberg, S.S. Abdullaev, S. Brezinsek, I. Classen, T.E. Evans, Y. Feng, K.H. Finken, M. Kantor, D. Reiter, U. Samm, B. Schweer, G. Sergienko, G.W. Spakman, M. Tokar, E. Uzel, R. Wolf, *Nuclear Fusion* 48 (2008) 024009.
- [36] W. Fundamenski, R.A. Pitts, J.E. contributors, *Plasma Physics and Controlled Fusion* 48 (2006) 109-156.

- [37] I.H. Hutchinson, B. LaBombard, J.A. Goetz, B. Lipschultz, G.M. McCracken, J.A. Snipes, J.L. Terry, Plasma Physics and Controlled Fusion 37 (1995) 1389-1406.

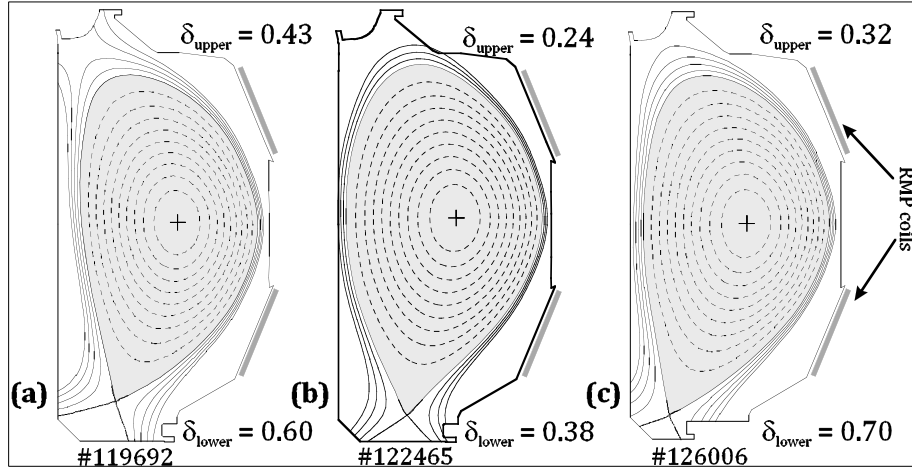


Figure 1. Examples of plasma shapes used to carry out H-mode RMP experiments: a-b) prior to February 2006, c) after February 2006

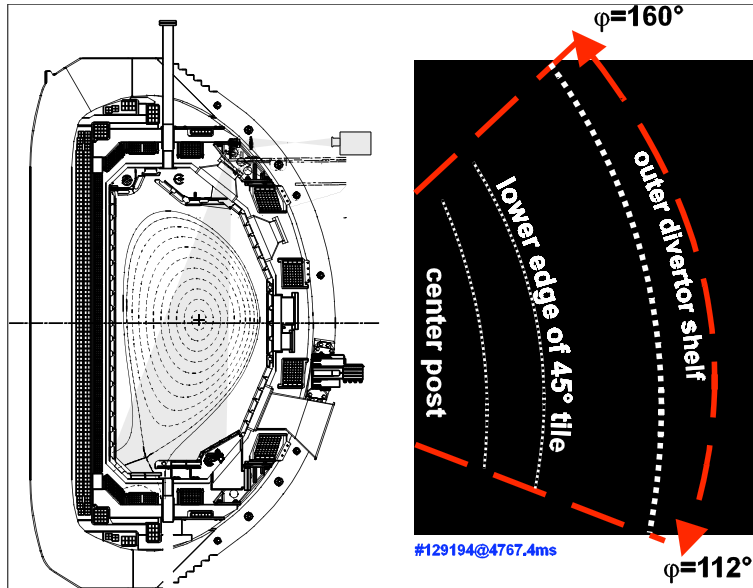


Figure 2. a) Sketch presenting infra-red setup allowing observation of lower divertor overlaid with equilibrium of the DIII-D discharge #129197. b) Snapshot of the lower divertor during the discharge taken by the infra-red camera SBF-125.

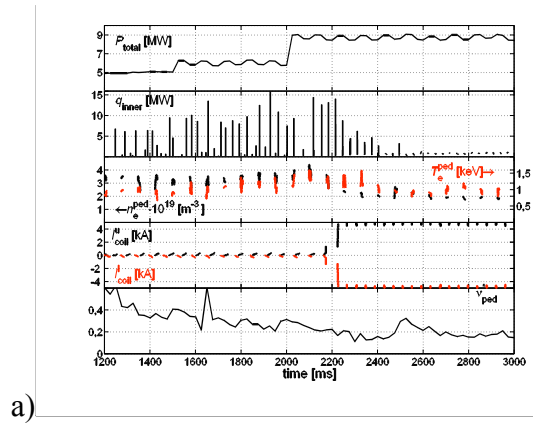


Figure 3. a) Overview of plasma parameters for the discharge #129197. From top of the graph: total heating power, power to the inner divertor, electron pedestal temperature and density, I-coil current and electron pedestal collisionality.

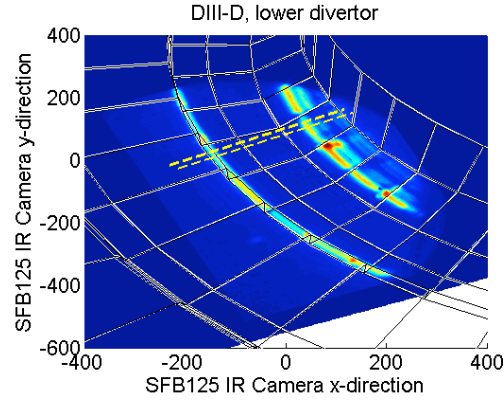


Figure 4. Infra-red image of the lower divertor taken during a Type-I ELM event. Yellow dashed lines indicate area, where heat flux density is evaluated

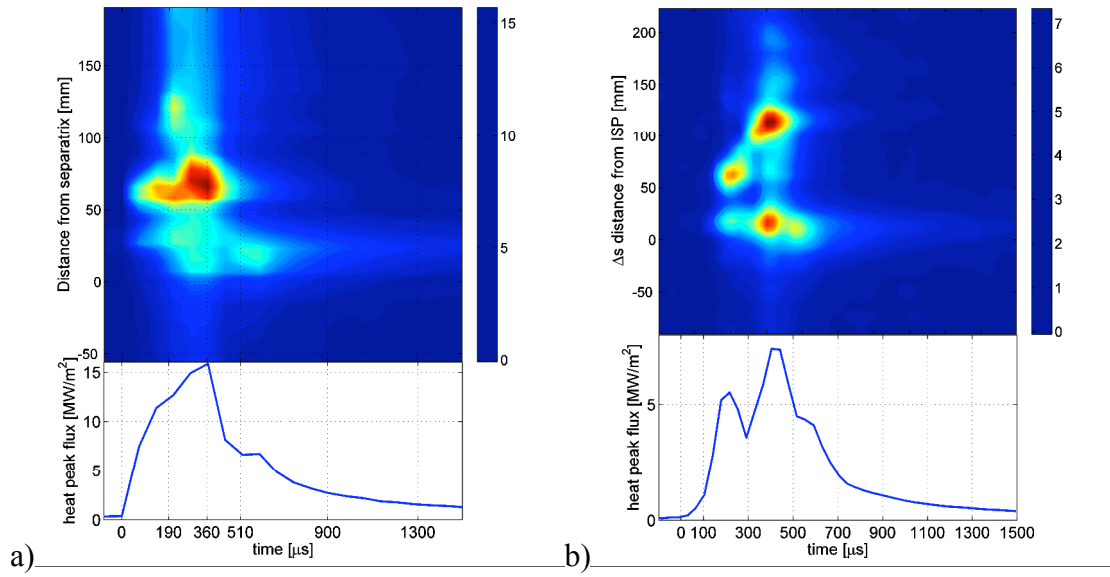


Figure 5. Evolution of the heat flux density at the inner strike point during two Type-I ELMs without RMP: (top) contour plot of heat flux density evolution at the inner strike point in false color representation (units in MW/m^2); (bottom) peak heat flux density vs. time for the same event



Figure 6. Energy deposited to the inner target due to ELMs. Each data point corresponds to one ELM event.

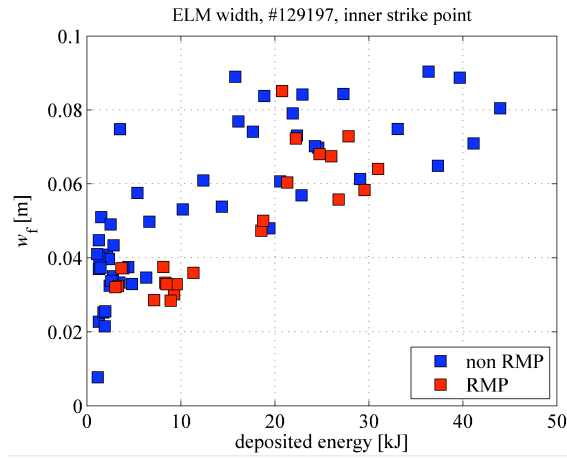


Figure 7. Wetted area of ELMs versus their size in terms of deposited energy to the inner target.

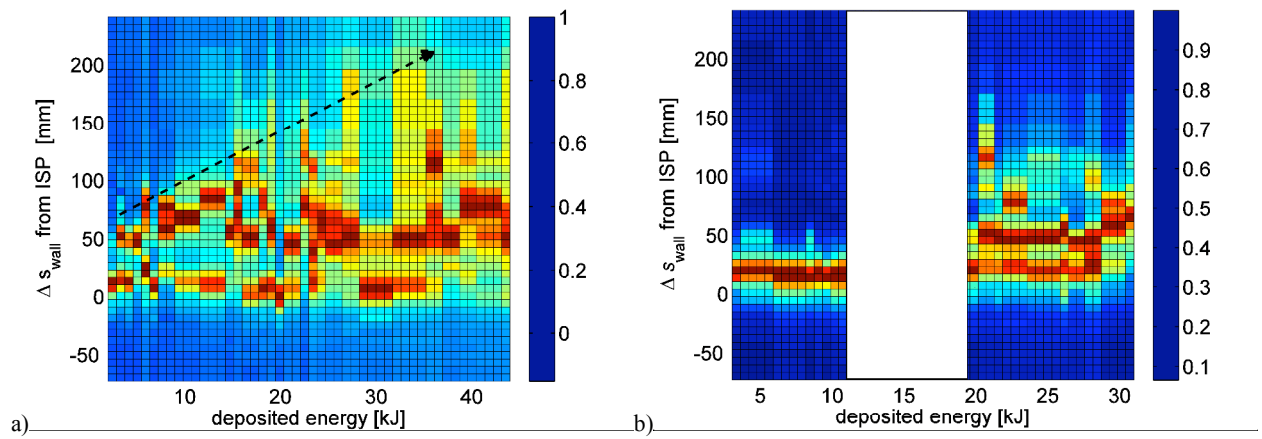
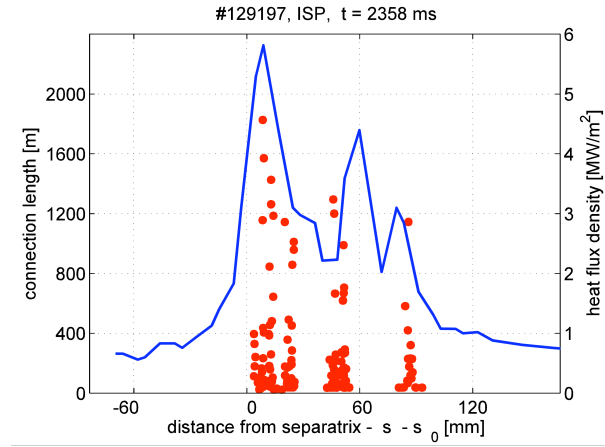


Figure 8. Profiles of ELM heatflux normalized to the peak heat flux value during non-RMP phase a) and during initial RMP phase b), where two groups of ELMs can be distinguished by the deposited energy (each vertical line corresponds to one ELM event). Therefore no ELMs at all exist in the energy range inside of the white box.



a)

Figure 9. Comparison of heat flux deposition pattern (blue curve, right ordinate) with predicted by TRIP3D connection length distribution (red dots, left ordinate).

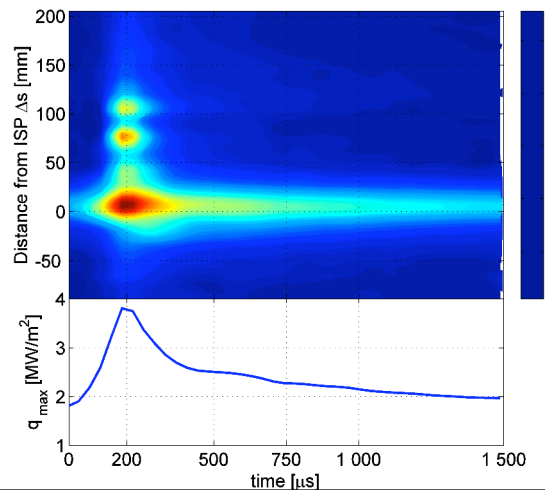


Figure 10. Evolution of heat flux density on the surface of the inner target during Type-I ELM in RMP phase: (top) contour plot of heat flux density evolution at the inner strike point in false color representation (units in MW/m²); (bottom) peak heat flux density vs. time for the same event.

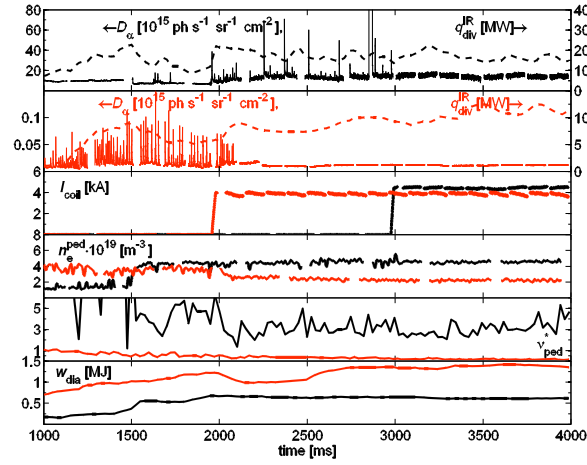


Figure 11. Plasma parameters for the discharges a) #119692 (black curves), 126006 (red curves). From top of the graph: divertor particle (solid) and heat flux (dashed) on top two graphs, I-coil current, pedestal electron density, pedestal collisionality, plasma stored energy.

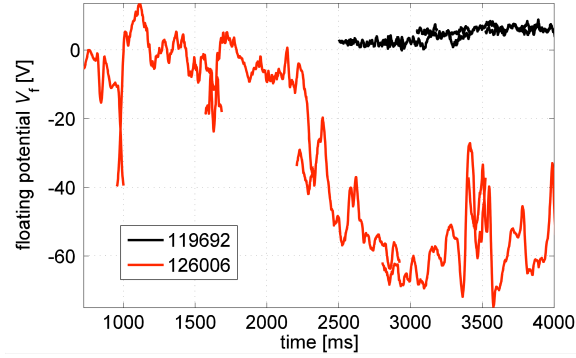


Figure 12. Floating potential measured by the Langmuir probe near the outer strike point for the same discharges as in **Figure 11**.

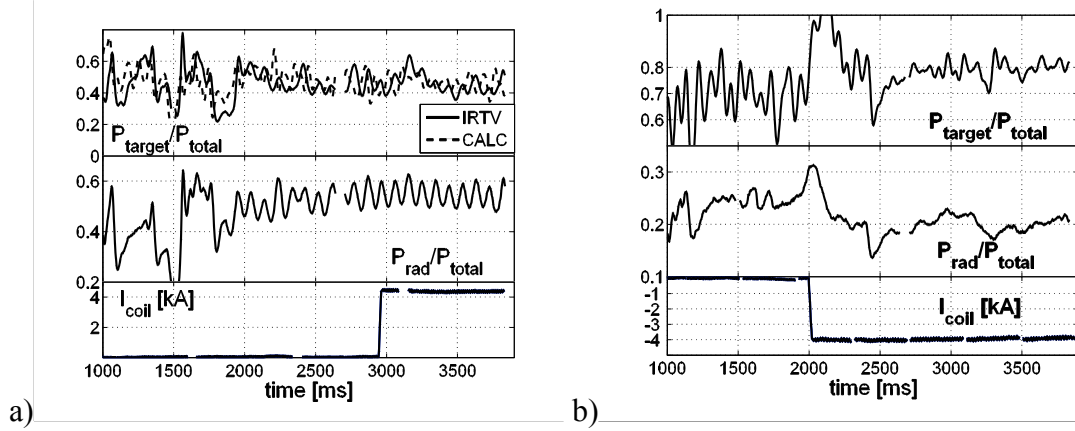


Figure 13. Power balance for the discharges #119692 (a) and #126006 (b). From top to bottom: total power to the divertor, total radiated power and I-coil current.

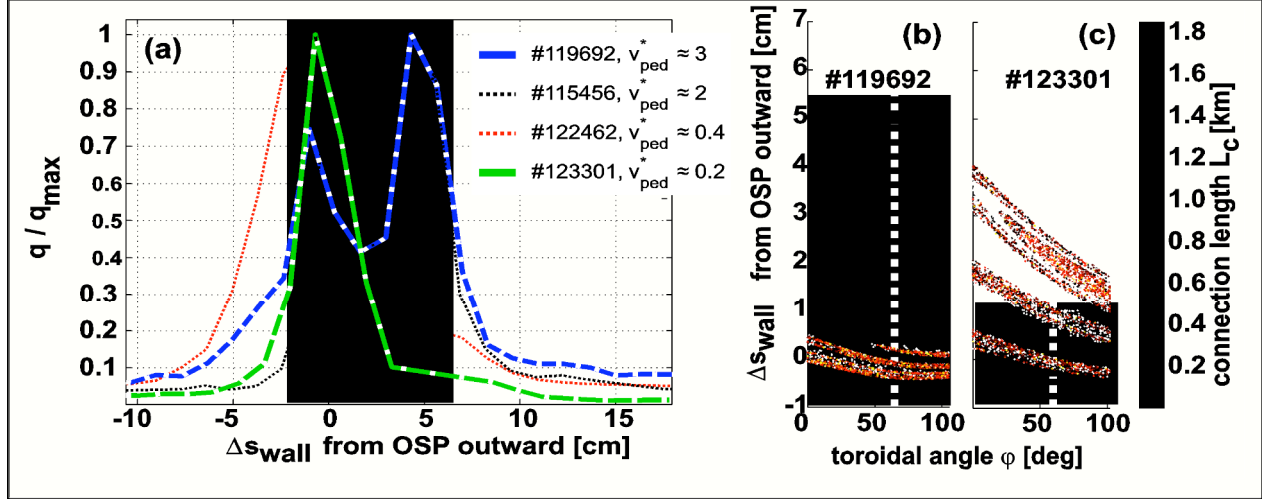


Figure 14. a) Profiles of the heat flux density measured by the infrared camera at the OSP. Profiles are taken during discharges with different collisionalities (see legend). Shaded areas indicate half width of the profiles (#119692 - purple, #123301 - green). b-c) Calculated with TRIP3D structure of the magnetic footprints on the divertor surface for #119692 (b) and #123301 (c). Green and purple shaded areas indicate width of the experimentally obtained heat flux profiles from (a)

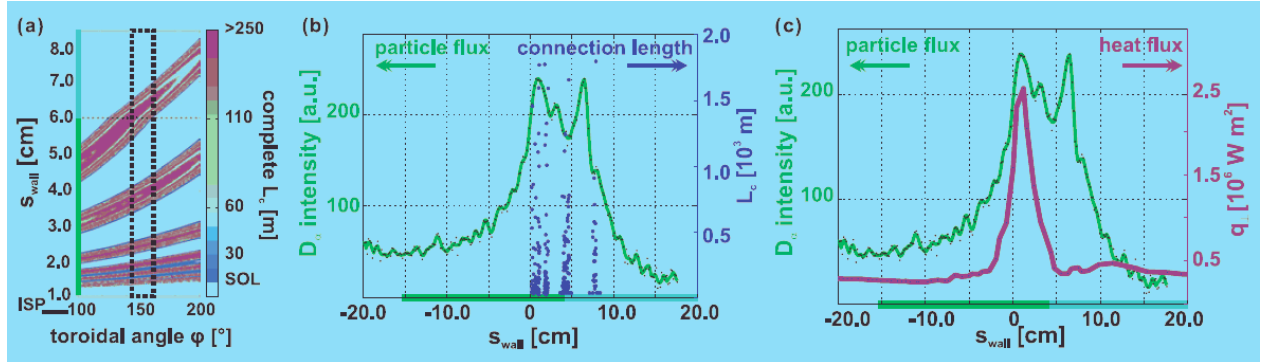


Figure 15. Identification of the perturbed separatrix striations on the inner divertor footprint pattern (reproduced from [9]). a) A cut of the magnetic footprint $L_c(\phi, s_{\text{wall}})$. b) A direct comparison of the particle flux profile (measured as $D\alpha$ intensity) with $L_c(s_{\text{wall}})$. (c) Depicts a direct comparison of the measured particle (green curve) and heat flux (red curve) profiles at the same toroidal angle.

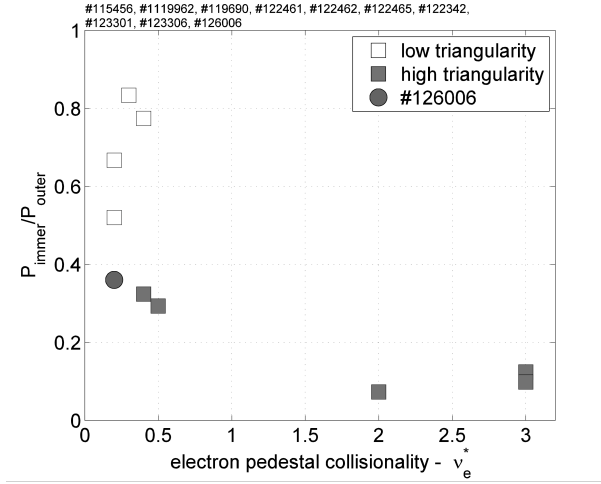


Figure 16. Asymmetries between power loads to the inner and outer strike line in the ELM suppressed phase of the discharge at different collisionalities and triangularities.